ARTICLE

Check for updates

Tracking the evolution of materials and interfaces in perovskite solar cells under an electric field

Juntao Hu[1,2,7], Peng Chen[3,7], Deying Luo [4✉], Dengke Wang[1], Nan Chen[1], Shiyu Yang[2], Zewei Fu[2], Maotao Yu[3], Lei Li[3], Rui Zhu [3,5,6✉] & Zheng-Hong Lu [1,4✉]

What causes the instability of perovskite solar cells has been a puzzling problem impeding the development of commercial panels. So far there is limited evidence on the link between device instability and the various materials in each of the stacked layers. Here, we study the chemistry and distribution of various species and the integrity of the functional layers in high-performance inverted perovskite solar cells, with and without an electric field. The distribution of the diffusion species and its impact on the chemical and electronic structures through the transporting layers are measured by photoemission spectroscopy combined with damage-free ion beam sputtering. We find that various species, such as I_2 and PbI_2, are distributed throughout the organic transporting layers toward the electrode interface. These species are found to be charge neutral, have no impact on the Fermi level, and react little with copper. An electric field, however, can catalyze the electro-decomposition of the perovskite, causing chemical heterogeneity and degradation in device performance.

[1] Department of Physics, Center for Optoelectronics Engineering Research, Yunnan University, 650091 Kunming, China. [2] Center of Development and Research, Yunnan Tin Group (Holding) Co. Ltd, 650106 Kunming, P. R. China. [3] State Key Laboratory for Artificial Microstructure and Mesoscopic Physics, School of Physics, Frontiers Science Center for Nano-optoelectronics & Collaborative Innovation Center of Quantum Matter, Peking University, 100871 Beijing, China. [4] Department of Materials Science and Engineering, University of Toronto, Toronto M5G 3E4 Ontario, Canada. [5] Peking University Yangtze Delta Institute of Optoelectronics, Nantong 226010 Jiangsu, China. [6] Collaborative Innovation Center of Extreme Optics, Shanxi University, Taiyuan 030006 Shanxi, China. [7] These authors contributed equally: Juntao Hu, Peng Chen. ✉email: deying.luo@utoronto.ca; iamzhurui@pku.edu.cn; zhenghong.lu@utoronto.ca

Planar heterojunction solar cells based on halide perovskites have gained considerable attention in recent years because they can be made with facile fabrication methods on various semiconductor substrates[1–4]. To date, the state-of-the-art PSCs have shown ever-increasing PCEs that are already comparable to monocrystalline silicon solar cells[5,6]. Yet, the poor operational stability for the PSCs has been a long-standing concern towards practical applications[7,8]. Although numerous encapsulation strategies have been developed to improve the operational stability against extrinsic factors (such as the damp-heat atmosphere) by protecting the perovskite from the atmosphere and avoiding chemical decomposition[9,10], the encapsulation cannot resolve the intrinsic instability issues[11,12]. Hence, enhancing intrinsic stability is currently one of the most important research topics for the PSCs. Previous studies speculate that the intrinsic stability is caused by ion migration leading to changes in material depth profile and at interfaces[13–16]. It has been reported that the presence of electric-assisted ion migration within the PSCs can cause a serious hysteresis in current-voltage curves when scanned from different directions at certain scan rates[17]. It has also been reported that the ion migration may exist in both hysteresis- and hysteresis-free PSCs, regardless of perovskite-contact interfaces[18]. Nonetheless, there is no direct experimental observation understanding electromigration and linking with the evolution of materials and interface in PSCs.

Thus, it is of particular importance in tracking the evolution of materials and interfaces in a real PSC under normal working conditions. At present, time-of-flight secondary ion mass spectrometry (ToF-SIMS), a technique that detects ionized species sputtered off a surface, has been the most common technique to analyze the depth distribution of chemical constituents throughout the PSCs[19–21]. ToF-SIMS, however, cannot detect the chemical and electronic structures of various matters in a PSC going from perovskite to charge-transport layers and to metal electrodes. As will be shown below that photoelectron spectroscopy, a surface analytical technique capable of measuring both chemical and electronic structures can be applied to obtain depth profiles of a PSC by combining damage-free layer-by-layer sputtering using gas cluster ion beam (GCIB)[22–24].

Herein, we report PES depth profiles of various materials and interfaces from perovskites to top metal electrodes of PSCs. The electric stress is stimulated by applying an external bias of ±1 V [which is equivalent to the voltage at maximum power point (MPP) of a PSC under a working condition] for 12 h (h). We have found that the depth profile of chemical constituents of different functional layers is as same as in bias-free cases, suggesting that the observed species in the organic transporting layers and at the interface are charge neutral. Previously it has been speculated that charged species may revert back to the perovskite layer when the electric field is removed[25,26], while the electrically passive species probably remain in the organic layer and at the contact interface. In addition, we also found that the chemical composition of the contact electrode interface remains unaltered by the external electric field. Instead, we discovered that, under electric stress, the perovskite starts to decompose, forming compositional heterogeneity on submicron/micron scales, as revealed in scanning electron microscopy (SEM) and X-ray diffraction (XRD) measurements.

Results and discussions

Chemical nature of diffused species in PSCs.
To fabricate the state-of-the-art inverted planar heterojunction PSCs, we employ the most commonly reported tri-cation mixed-halide perovskites $(Cs_{0.05}FA_{0.85}MA_{0.10})_{0.95}Pb(I_{0.85}Br_{0.15})_3$, where FA and MA are formamidinium and methylammonium, respectively. Figure 1a (inset) presents the device configuration of inverted planar

heterojunction PSCs, and outstanding device performances (PCE > 21%) shown in Fig. 1a and Supplementary Table 1 ensure high-quality perovskite absorbers and interfaces and contact electrodes throughout this work. To probe the depth distribution of chemical constituents across multilayer stacks, the bias was loaded to simulate the actual operating situation at the MPP. According to the scanned current density–voltage results, as shown in Fig. 1a, ±1 V (i.e., the absolute value equals to the voltage at the MPP) was applied to the PSCs for 12 h (Fig. 1b), of which electromigration of mobile species would be triggered if those of mobile species are positively and/or negatively charged ions, as widely believed. In order to track changes in chemical constituents and energy bands of the functional layers and interfaces, XPS/UPS depth profile measurements are made on a buried copper electrode surface peeled off from the PSCs in a N_2 glove box (H_2O, 0.04 ppm; O_2, 0.7 ppm). The glove is linked to the XPS/UPS chamber so that samples can be transferred in-situ without being exposed to ambient atmosphere. The details on the Cu electrode cleavage using methods are described in detail elsewhere[27]. The two surfaces created by the cleavage are used to conduct depth-dependent XPS and UPS surface analyses (Fig. 1c).

To measure the exact chemical states for all possible diffused species, we track the depth evolution of four representative elements for the BCP side (N, C, I, and Pb) and the cleaved Cu side (N, I, Pb and Cu). Figure 1d–f compares the variation of these elements on the BCP side cleaved from the full PSCs with various electric stresses (0 V, −1 V, and +1 V). On the as-cleaved surfaces (0 s, without any GCIB sputtering), all the samples with and without electric stresses show the same characteristic XPS spectra of N 1 s, C 1 s, I 3d, and Pb 4 f. After sputtering, peak positions show a slight shift but the overall depth profiles of these elements are identical for these three samples. The bias independence of these elemental depth distributions suggests that those species are charge neutral. Further analysis shows that the only peak at 398.6 eV (initial time, 0 s) from the N 1 s spectrum is the =N- groups from the BCP molecules. This peak (i.e., BCP), disappears after 60 s GCIB sputtering. For the C 1 s spectra, the initial full width at half maximum (FWHM) ~1.06 eV of an asymmetric peak decreases to 0.94 eV after 60 s sputtering. The FWHM remains at 0.85 eV for the rest of the sputtering time. This change in the FWHM of C 1 s XPS spectra indicates the transition from the BCP layer to the PCBM layer, and the estimated BCP thickness is ~3.6 nm. It is worth noting that MA and FA cations with their respective signature N 1 s peaks at ~402.5 eV and ~400.8 eV, and C 1 s peaks at ~286.5 eV and ~288.4 eV[28], have not been detected. We have not detected in the organic layers the N-containing species from the MA and FA cations. It is possible that the decomposed N-containing species are volatile compounds that may readily vaporize in atmosphere[29].

Notably, both Pb 4 f and I 3d signals are detected throughout the thickness of PCBM/BCP bilayers, even on the as-cleaved BCP surface before sputtering. These results suggest that the detected Pb and I species in the BCP and PCBM layers are from chemical species diffused from the underlying perovskite. Meanwhile, we note that external electric fields induce little change in these Pb 4 f and I 3d signals, indicating that these species are electrically passive. In order to identify the chemical states associated with the detected I 3d and Pb 4 f, we measured the XPS spectra of standard PbI_2 powders, as shown in Supplementary Fig. 2. In contrast to the standard PbI_2 XPS spectra, we found that the energy spacing between I 3d and Pb 4 f (from 60 s) for XPS signals obtained from the cleaved BCP side is identical to that recorded from the standard PbI_2, even though a shift in absolute binding energy (BE) is observed and expected as due to different Fermi levels in these two samples. Note that the absolute binding
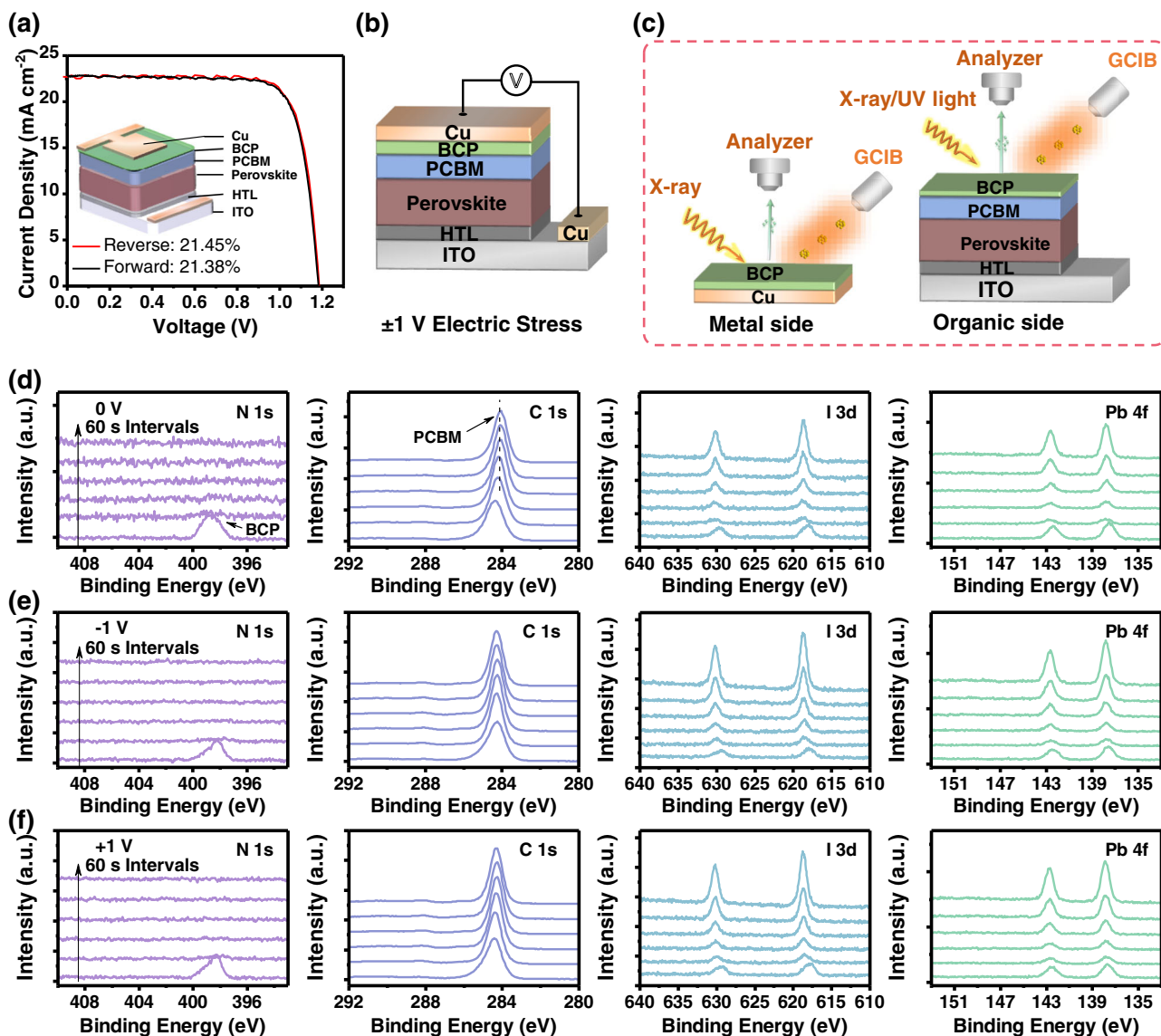
Fig. 1 Device performance and XPS depth profiles. a Typical *J–V* curves for the inverted planar heterojunction PSCs from both the forward and reverse scans. (Inset) A PSC consists of glass/ITO (indium tin oxide)/HTL (8 nm)/perovskite (500 nm)/PCBM (30 nm)/BCP (8 nm)/Cu (100 nm). HTL, hole transporting layer. PCBM (phenyl-C61-butyric acid methyl ester, $C_{72}H_{14}O_2$) and BCP (bathocuproine, $C_{26}H_{20}N_2$) are the electron transporting and hole blocking layers, respectively. **b** Schematic illustration of the PSCs with the electric stress of ±1 V. The whole process was conducted in a dark N_2-filled glove box without exposure to air. **c** Illustration of two surfaces cleaved from the same device for depth-dependent XPS and UPS analyses. **d–f** Depth XPS profiles for the BCP side cleaved from the full PSCs with and without electric stress: **d** 0 V, **e** −1 V and **f** +1 V. The XPS depth profiles for the BCP side with and without electric stress are provided in Supplementary Table 2. Note that the metallic Pb (Pb^0) was observed from the XPS spectra once sputtering the perovskite absorber (Supplementary Fig. 1).

energies for I 3d XPS spectra cannot serve as a fingerprint to distinguish ions or molecules[30], so we need to quantify atomic/molar ratios across multilayer stacks in the next section.

Electric field on depth profiles of I_2 and PbI_2. Figure 2a presents the atomic ratio of Pb and I as a function of the GCIB etching time whereby reflects the depth profile of chemical constituents across multi-functional layers. With an increase in the sputtering time, there is a considerable rise in the I atomic ratio (<120 s) whilst exhibiting a decrease with the etching time over 180 s. However, the Pb atomic ratio for the bias-free samples shows an opposite trend regardless of electric stresses. Further, we find that the total I atomic ratio for three samples applying various electric stresses (0 V, −1 V, and +1 V) are much higher than that of the

PbI_2 power, indicating that mobile species could include pure I_2 as well. Otherwise, the inclusion of I^- within multilayer stacks would result in enhanced or weakened I atomic ratios under bias conditions in comparison to the bias-free sample. It has been suggested that molecular I_2 may come from the redox I^-/I_2 reaction under bias conditions[31]. This redox reaction, if any, is expected to be a minor process as the I atomic ratios are found to be the same in all samples regardless of bias conditions.

To further assess the impact of electric fields on the distribution of diffused species, we first analyze the depth distribution of I_2 and PbI_2 at different functional layers with the depth-dependent XPS data. As shown in Fig. 2b, the molar ratios of N (marked as BCP) and C (marked as PCBM) obtained from the depth-dependent XPS spectra indeed show an abrupt change, as expected in the layer-by-layer structures of PCBM and
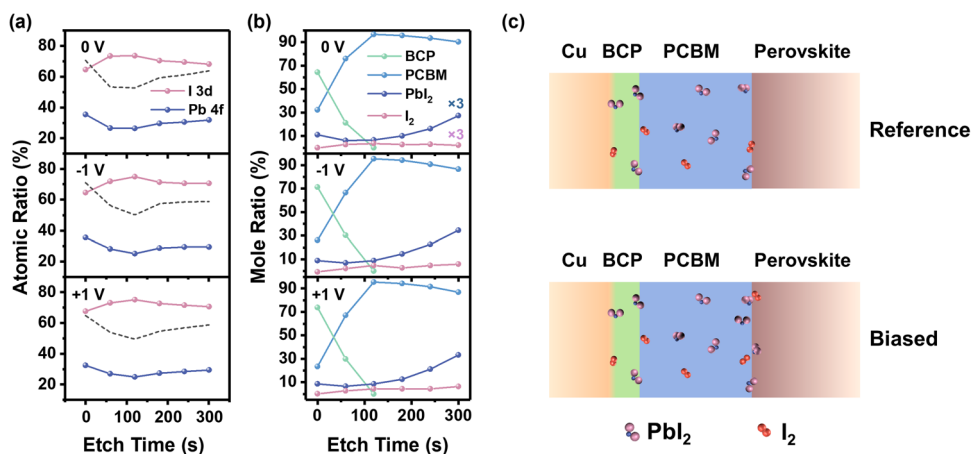
3

Fig. 2 The chemical constituent distributions as a function of sputtering time. a The relative concentration of Pb and I for the samples with and without electric stress (±1 V). The data points are based on two sets of samples. The sample-to-sample uncertainty is ±0.7% (0 V), ± 0.4% (−1 V) and ±0.4% (+1 V), respectively (seen in Supplementary Table 3). The dashed gray dash line represents the I stoichiometric ratio for the PbI_2. **b** The molar ratios of the chemical constituents extrapolated from the elemental depth profile in Fig. 1b–d. **c** Schematic diagram of mobile species throughout the multilayer stacks consisting of perovskite/PCBM/BCP/Cu. Mobile species such as PbI_2 and I_2 are marked as well.
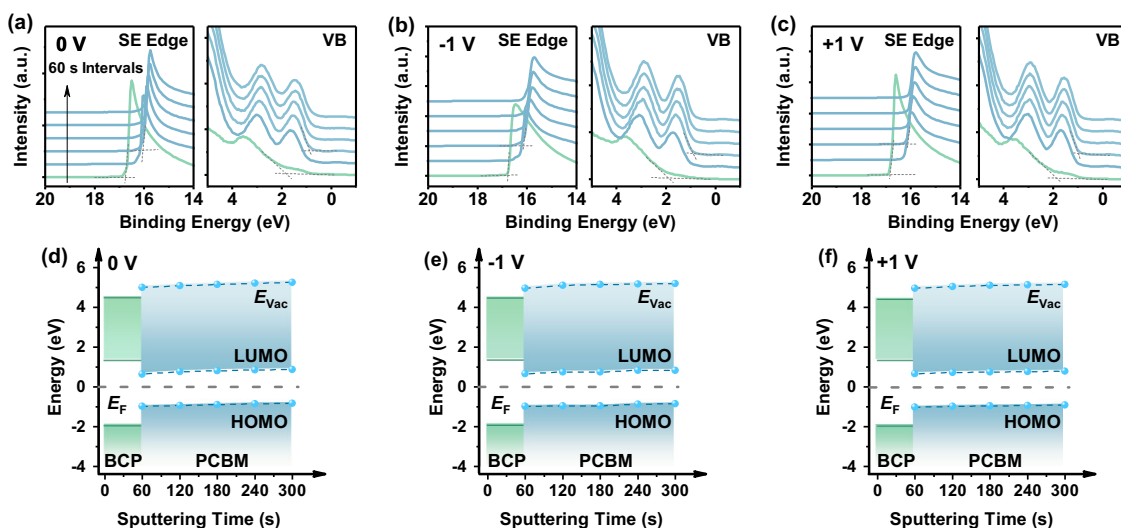

Fig. 3 Depth-dependent UPS spectra and energy bands. a–c Helium Iα ($hv = 21.22$ eV) spectra of the secondary electron cutoff (SECO) (right) and valence band (VB) (left) of PSCs with the electric stress (0 V, −1 V, and +1 V). Note that the HOMO and φ are determined by line extrapolation of the leading edge. **d–f** The energy bands taken from the above UPS measurements: **d** 0 V, **e** −1 V, and **f** +1 V. HOMO, the highest occupied molecular orbitals. LUMO, the lowest unoccupied molecular orbitals. E_F is the Fermi level. E_{vac} is the vacuum level.

BCP in device stacks. Regarding the PbI_2 content at different functional layers, it is found that the PbI_2 is decreased in the BCP layer and then increased when entering the PCBM layer. The relative contents of PbI_2 (after 300 s etching) for the three samples under the various electric stresses are 9.1% (0 V), 11.3% (−1 V) and 11.1% (+1 V), respectively. This suggest that electric fields have induced an increase in the PbI_2 in the PCBM region close to the perovskite. Likewise, I_2 contents show a similar variation, with relative contents of 0.7%, 1.9%, and 2.1% after 300 s etching.

Electric field on Fermi levels and band alignments. As the PbI_2 and I_2 are distributed throughout the thickness of the PCBM/BCP stacks, we now move on to exploring the influence of these chemical constituents on energy bands and contact electrodes. The UPS depth profiles of these samples are shown in Fig. 3a–c. On the BCP side of the cleaved surface from a bias-free device (Fig. 3a), the edge of the highest occupied molecular orbitals (HOMO) and work function (φ) is determined to be −1.92 eV

and 4.47 eV, respectively. Also, it is noted that the PCBM's HOMO feature is detected. This indicates that the BCP layer is very thin or has minimal PCBM exposure. After sputtering at 60 s intervals, the HOMO and secondary electron cutoff (SECO) edges are both changed in the UPS spectra. The onset of the HOMO has shifted to −0.97 eV and the φ to 5.00 eV. With further sputtering, the change in both the valence band (VB) and SECO edges are very small. To be specific, the HOMO upshifts from −0.93 eV to −0.83 eV, and the φ increase from 5.09 eV to 5.25 eV, on the sample with sputtering cycles from 120 s to 300 s, respectively. Following the evolution of the VB and SECO edges with the GCIB sputtering and depth-dependent bandgaps determined by reflection electron energy loss spectroscopy (REELS) in Supplementary Fig. 3[32], we construct the energy band profiles across the PCBM/BCP interfaces for the bias-free sample, as shown in Fig. 3d. As for the samples with the electric stress, we note that the evolution of the VB and SECO edge is the same as the bias-free sample (Fig. 3b and Fig. 3c), and corresponding energy bands
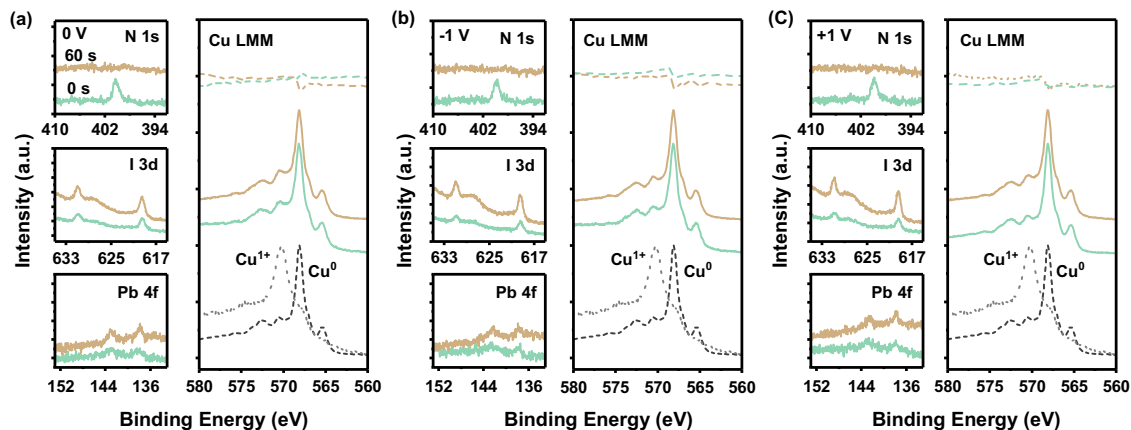
Fig. 4 Depth-dependent XPS profiles for the cleaved Cu electrode side. a–c The distributions of N, I, Pb, and Cu for PSCs with and without electric stress. **a** 0 V, **b** −1 V, and **c** +1 V. The difference spectra (raw data minus Cu^0 reference spectrum[55], noted as the dashed line in the Cu LMM graph) show the Cu electrode are mainly Cu^0 feature, indicating the Cu electrode is not affected by the diffused I_2 significantly. The differentiation between metal and oxides of copper's chemical states is indistinguishable in Cu 2p XPS spectra. Thus, the Cu LMM Auger spectra are used to help assign chemistry[56]. The Cu $2p_{3/2}$ spectra of these corresponding samples are provided in Supplementary Fig. 4.

are displayed in Fig. 3e and Fig. 3f. The above results suggest that the probed chemical species are electronically passive, affecting little the Fermi levels in the organic transport materials and alignment of energy bands at the PCBM/BCP interface.

Chemical structures at contact electrode interfaces. Now let us examine whether the I-containing molecules influence the integrity of metal electrodes. To this end, we study the Cu metal electrode by analyzing the chemical constituents of the cleaved Cu side, focusing on electric stresses. The as-cleaved Cu surface shows N 1 s (at 400 eV) XPS signals (Fig. 4a), implying that a thin BCP layer is attached to the Cu side. It is noted that the BE of these N 1 s differs by 1.4 eV from that detected on the BCP side of the cleaved device. This is due to the difference in work functions of the substrates used in these two samples. This ultrathin BCP layer can be sputtered off by 60 s GCIB sputtering, indicating the thickness of BCP on Cu electrode is <3.6 nm, as shown in Fig. 4a (upper). With the elimination of this BCP overlayer, both I 3d and Pb 4 f XPS signals are enhanced whilst maintaining the same binding energies as shown in Fig. 4a (middle, bottom). These observations suggest that I-containing molecules such as PbI_2 and I_2 are accumulated at the metal electrode/BCP interface. Those molecules, however, show no detectable chemical reaction with the Cu electrode as LMM Auger spectra show only the Cu^0 signals, as shown in Fig. 4a (right). Further, for the electric-stressed (±1 V) PSCs, we cannot find any additional XPS peaks that may come from different states (Fig. 4b and Fig. 4c). This indicates that there is no significant I_2 electrochemical corrosion under the electric field. It is possible that the low iodine concentration (Supplementary Table 4) may not lead to any detectable chemical/electrochemical reaction products on the electrode surface. Based on thermodynamic consideration, a corrosion reaction may occur when I_2 is in direct contact with Cu[33], seen in Supplementary Table 5. Nevertheless, the corrosion action of diffused iodine on Cu electrode in optimized high-performance PSCs is negligible.

We now examine the diffusion of electrode metal deposited by physical vapor deposition. The presence of diffused Cu in multilayer stacks necessitates the use of the multimodal XPS technique for studying its depth distribution. The Cu 2p core level and Cu LMM Auger spectra are provided in Supplementary Fig. 5. The XPS depth profiles show that a trace amount of Cu, ~0.6 at.%, has penetrated into the BCP/PCBM bilayer. The

penetration depth is ~18 nm, estimated by the disappearance of the Cu signal after 300 s sputtering. In the case of the biased samples, the same amounts of Cu (~0.6 at.%) are detected. Some of the diffused Cu may have reacted with the I_2 to form CuI, as hinted by a weak Cu^+ LMM Auger line at ~570 eV (shown in Supplementary Fig. 5b). The observation of identical Cu 2p and LMM depth profiles for all samples, however, indicates that these species are most likely formed during electrode deposition.

Electric field catalyzed perovskite decomposition. A general consensus has been that the stability assessment for the PSCs must consider the long-term operational stability at the MPP under sunlight illumination[34]. Numerous studies have shown that the stability degradation at MPP tracking (electric stress under sunlight illumination) is the fastest among all the stresses (damp-heat, light, and so on)[8,35]. Thus, the stability assessment must consider electric fields. Our results indeed demonstrate that after applying the electric stress for 5 h, the stabilized power output (SPO) for positively biased PSCs at MPP tracking degraded to a lower level in a short time while negatively biased PSCs show a negligible decrease in Fig. 5a and Fig. 5b. The resulting PSCs, however, show consistent device performances evaluated from the scanned J–V results as shown in Supplementary Fig. 6 and Supplementary Table 6–7. As discussed above, the detected chemical species (I_2 and PbI_2) in different functional layers of the PSCs, with or without electric field, have no impact on the Fermi level of the organic transport layers and band alignment at the organic transport layer interfaces, and the Cu contact electrode. Thus, we turn to study the integrity of the perovskites under electric stress.

To this goal, we further analyzed the evolution of the microstructures and crystal structures of perovskite absorbers cleaved from the full PSCs with and without electric stress. From SEM images (Fig. 5d), we observe that, in contrast to the bias-free perovskite, white features on the perovskite surface are greatly enhanced for the positively biased perovskite. These features, however, show only a slight increase for the negatively biased perovskite. The cross-sectional SEM images (Supplementary Fig. 7), however, show that the grain structures are similar for these samples. These white grain features observed from the SEM images are ascribed to lead-halide compounds[36], as evidenced by consistent enhancements of XRD patterns (Fig. 5c), and the trends observed in the SEM and XRD are in agreement with the XPS results (i.e., PbI_2 rich on the perovskite surface for the +1 V
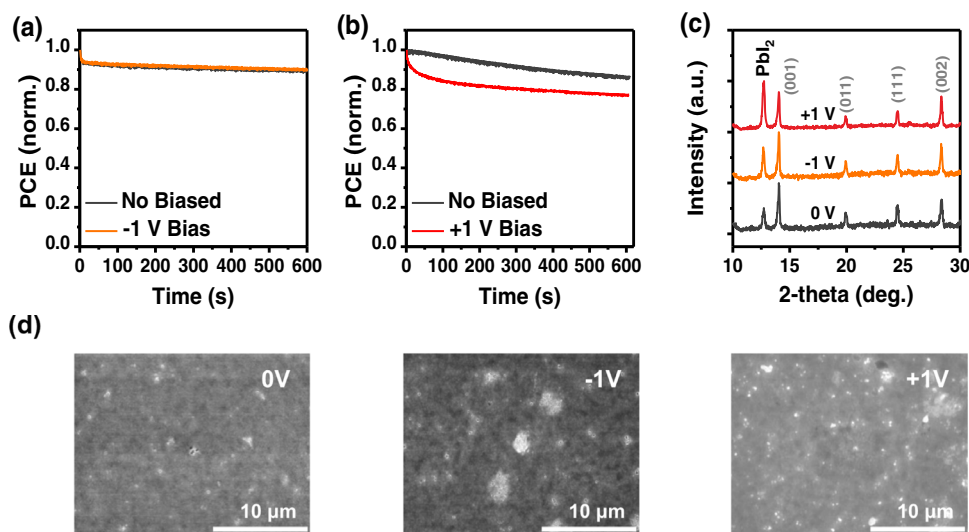
Fig. 5 SPO, XRD and SEM images. Comparisons of the SPOs for the PSCs tracking at the MPP before and after applying electric stress: **a** −1 V and **b** +1 V. **c** XRD patterns for the samples cleaved from the full device with and without electric stress (0 V, −1 V, and +1 V for 12 h). **d** Top-view SEM images of the corresponding cleaved samples.

based sample). These observations are consistent with several reports using transmission electron microscope (TEM) to study devices under bias stresses[37,38]. The increase in the lead-halide phases or compounds under electric stress (+1 V) suggests that electro-decomposition in the perovskite can cause degradation in device performance when the PSCs operate under normal working conditions. Despite impressive defect passivation of PbI_2 in the perovskite deposition by solution processing[39], recent studies have now shown that submicron-scale lead-halide phases present within the perovskite bulk and on the surfaces are the predominant factor for introducing nanoscale and/or submicron scale deep-state defects[40], which in turn accelerates stability degradation under the working conditions and lowering device lifespan[41–43]. Hence, it is expected that mitigating electro-decomposition of the perovskite absorber will become an increasingly important research subject.

It should be pointed out that our findings of charge-neutral species distributed in the organic transporting layers and at the interface contradict the current consensus that the diffusion species in PSCs are ions. In these previous literatures, the conclusion of ion diffusion in the PSCs is deduced based on various measurements using techniques such as transient capacitance[44,45], photoluminescence (PL)[46–48], ToF-SIMS[33,49], and so on[50,51]. Among them, the ToF-SIMS is the only analytical technique directly measuring the chemical species sputtered off a PSC sample. Due to the nature of the mass spectrometer, the measured species are either positively charged or negatively charged rendered by energetic sputtering ion beams. The measured ionized species do not represent the chemical structure of these species in a material. For example, both positively and negatively charged aluminum clusters can be produced from a metallic Al sample and are used to analyze its concentration in a material[52,53]. In our case, the GCIB beam has been shown to sputter materials without causing changes in molecular structure or reactions[54]. The metallic lead, a typical X-ray radiation-damaged product during in-situ photoemission spectroscopy measurement, was not detected in our samples. So the observed species in the organic transporting layers and at the interface are unlikely to result from sputtered and/or radiation damage by-products. Other techniques such as capacitance and PL measure convoluted changes of materials from all stacked layers. As shown in Fig. 5 the external electric bias, in additional to built-in

potential, can enhance the decomposition of the perovskite. The decomposition may create more charged vacancies and inter-stitials in the perovskite layer. It is quite possible that these previously observed phenomena are likely caused by the biased-induced species in the perovskite layer. It is, however, very difficult to measure these variations directly by XPS depth profile as the sputtering cluster Ar^+ ions beam will damage the rather fragile perovskite creating artifact defects.

Conclusion

In summary, we have studied the chemical nature and depth distribution of various species in high-performance PSCs with and without electrical stress. Using depth-dependent XPS/UPS/REELS, we have determined that trace amounts of PbI_2 and I_2 are remained everywhere from the electrode to the perovskite surface. These probed species have been shown to be electrically and electronically passive, so they neither migrate under electrical field nor affect Fermi levels and band alignment in the device. We also find no evidence of chemical corrosion by I_2 to form CuI at the Cu/organic interface. Based on SEM and XRD analysis of the PSCs with and without electric stress, we show that the device degradation arises from a considerable increase in PbI_2 in the perovskite induced by electro-decomposition under the external electric stress. These findings provide clear data on the stability of various materials in the PSCs under electric stress and should help guide researchers in developing more robust functional materials and devices.

Methods

Materials and reagents. Bathocuproine (BCP) and Poly [bis (4-phenyl) (2, 4, 6-trimethylphenyl) amine] (PTAA) (Mn ≈ 12,000) were purchased from Xi'an Polymer Light Technology Corp (China). Formamidinium iodide (FAI) and methylammonium bromide (MABr) were purchased from Greatcell Solar. Cesium iodide (CsI, >99.99%) was purchased from Sigma-Aldrich (USA). Potassium iodide (KI, ≥ 99.5%) was purchased from Sigma-Aldrich (USA). Lead dibromide ($PbBr_2$, 99%), lead diiodide (PbI_2, 99%), and choline bromide (CBR) were pur-chased from TCI (Japan). [6,6]-phenyl-C61-butyric acid methyl ester (PCBM) was purchased from Nano-C Tech. (USA). Copper (Cu) was purchased from a com-mercial source with high purity. Isopropanol (IPA), ethanol, chlorobenzene (CB), dimethylformamide (DMF), and dimethyl sulfoxide (DMSO), were purchased from commercial sources (Acros). Toluene was purchased from Sinopharm Che-mical Reagent Co., Ltd (China). All reagents were used as received without further purification.

Device preparation. The PSC devices studied were fabricated on an indium tin oxide (ITO) substrate. ITO glasses were cleaned through sequential ultrasonication in soap water, deionized H_2O, acetone, and isopropanol for 20 min each followed by 10 min of UV − ozone treatment. The PTAA layer was spin-coated (5000 rpm, 30 s) onto the ITO-coated glass substrate, and then annealed at 120 °C for 10 min. A modified layer of PEAI was deposited before spin-coating the perovskite layer. The PEAI solution (10 mg mL^{-1} in IPA) was spin-coated onto the PTAA layer at 5000 rpm for 30 s, and samples were then heated at 100 °C for 5 min. The perovskite precursor solution was prepared by mixing PbI_2 (1.28 M), FAI (1.21 M), MABr (0.16 M), $PbBr_2$ (0.22 M), and CsI (0.07 M) in the mixed solvent (DMF/DMSO) with volume ratio of v/v = 4:1. The perovskite layer was fabricated by a two-consecutive step program at 2000 rpm for 10 s and 6000 rpm for 30 s, respectively. At the final 16 s of the spin-coating process, 100 µL CB was dropped on the center of the spinning substrates to remove the remaining solvent. The samples were then annealed at 105 °C for 60 min. The top CBR (2 mg mL^{-1} in IPA) modification layer and PCBM (20 mg mL^{-1} in CB) electron transport layer were prepared with the speed of 5000 rpm for 30 s and 1000 rpm for 30 s, respectively. BCP (1 mg mL^{-1} in ethanol) was spin-coated at 5000 rpm for 30 s. Finally, the Cu (100 nm) electrode was deposited by thermal evaporation to complete device fabrication.

Characterization and measurement

Applying electric stress. The positive and negative electric stress with an amplitude of 1 V were loaded on two PSCs using Keithley 2400 Source Meter. These two biased devices from the same PSCs to avoid sample-to-sample variations. For the characterization, the Cu electrodes of the PSCs were peeled off using the carbon tape after loading the bias for 12 h. All the above processes were operated in the N_2-filled glove box. After that, the cleaved samples were introduced into the PES chamber via a vacuum transfer module and performed PES measurements. For the regular tests, the samples were stored in an N_2-filled transfer box before loading into the instruments.

Characterization. The PES measurements were performed on the Thermofisher ESCALAB Xi$^+$ system. For reference, the XPS/UPS spectra energy positions were calibrated using a standard Au sample (seen in Supplementary Fig. 8). The GCIB sputtering with 2000 sizes at 4 keV mode, at which the sputtering ratio is about 0.6 nm s^{-1}, was used to remove the organic layers. XPS measurements were carried out using monochromated AlKα source ($hv = 1486.6$ eV) with a pass energy of 20 eV. UPS measurements were performed using a He UV lamp ($hv = 21.2$ eV) with a pass energy of 1 eV. The XPS and UPS sampling depths are ~10 nm and ~2 nm for the organic films, respectively. The removed thickness in total for 300 s sputtering is estimated to be ~18 nm of the organic layer which allows us to detect the 0–28 nm depth chemical profiles from the as-cleaved organic surface to the PCBM layer. In our study, the thickness of the PCBM layer is ~30 nm. REELS measurements were acquired using a 1 keV electron beam with a pass energy of 6 eV. SEM images were collected by a field-emission scanning electron microscopy (Hitachi U8010) under upper detection [SE(U)] mode, with a 15-20 keV accelerating voltage for microscopy scan and 2 keV accelerating voltage for the cross-sectional scan. The XRD patterns were acquired using the Rigaku Ultima IV XRD system with Cu Kα radiation (λ = 1.54 Å) at 3 degrees per min scanning speed.

Device Measurement. The device performances were tested using a Keithley 2400 Source Meter under AM 1.5 G irradiation from a Xenon-lamp solar simulator (XES-40S1, SAN-EI). Prior to device tests, the light intensity of 100 mW cm^{-2} was calibrated using a standard monocrystalline silicon solar cell with a KG-5 filter. The current density–voltage (J–V) characteristics were measured under a forward scan from −0.02 V to 1.21 V and a reverse scan from 1.21 V to −0.02 V with no decay time. The SPO measurement was conducted tracking at the MPP under 1-sun sunlight illumination.

Data availability

The data that support the findings of this study are available from the corresponding author upon reasonable request.

References

1. Liu, M., Johnston, M. B. & Snaith, H. J. Efficient planar heterojunction perovskite solar cells by vapour deposition. *Nature* **501**, 395–398 (2013).
2. Luo, D. et al. Enhanced photovoltage for inverted planar heterojunction perovskite solar cells. *Science* **360**, 1442–1446 (2018).
3. Jiang, Q. et al. Surface passivation of perovskite film for efficient solar cells. *Nat. Photon.* **13**, 460–466 (2019).
4. Zhang, B. et al. NiO/perovskite heterojunction contact engineering for highly efficient and stable perovskite solar cells. *Adv. Sci.* **7**, 1903044 (2020).
5. Jeong, J. et al. Pseudo-halide anion engineering for alpha-FAPbI₃ perovskite solar cells. *Nature* **592**, 381–385 (2021).
6. Min, H. et al. Perovskite solar cells with atomically coherent interlayers on SnO₂ electrodes. *Nature* **598**, 444–450 (2021).
7. Liu, D. et al. Strain analysis and engineering in halide perovskite photovoltaics. *Nat. Mater.* **20**, 1337–1346 (2021).
8. Bai, S. et al. Planar perovskite solar cells with long-term stability using ionic liquid additives. *Nature* **571**, 245–250 (2019).
9. Cheacharoen, R. et al. Design and understanding of encapsulated perovskite solar cells to withstand temperature cycling. *Energy Environ. Sci.* **11**, 144–150 (2018).
10. Huang, C.-K. et al. Flip-chip packaged perovskite solar cells. *Energy Technol.* **9**, 2001129 (2021).
11. Wang, Y., Arumugam, G. M., Mahmoudi, T., Mai, Y. & Hahn, Y.-B. A critical review of materials innovation and interface stabilization for efficient and stable perovskite photovoltaics. *Nano Energy* **87**, 106141 (2021).
12. Guo, R. et al. Degradation mechanisms of perovskite solar cells under vacuum and one atmosphere of nitrogen. *Nat. Energy* **6**, 977–986 (2021).
13. Yuan, Y. & Huang, J. Ion migration in organometal trihalide perovskite and its impact on photovoltaic efficiency and stability. *Acc. Chem. Res.* **49**, 286–293 (2016).
14. Wei, D. et al. Ion-migration inhibition by the cation-π interaction in perovskite materials for efficient and stable perovskite solar cells. *Adv. Mater.* **30**, 1707583 (2018).
15. Rivkin, B. et al. Effect of ion migration-induced electrode degradation on the operational stability of perovskite solar cells. *ACS Omega* **3**, 10042–10047 (2018).
16. Li, C. et al. Iodine migration and its effect on hysteresis in perovskite solar cells. *Adv. Mater.* **28**, 2446–2454 (2016).
17. Le Corre, V. M. et al. Quantification of efficiency losses due to mobile ions in perovskite solar cells via fast hysteresis measurements. *Sol. RRL* **6**, 2100772 (2022).
18. Calado, P. et al. Evidence for ion migration in hybrid perovskite solar cells with minimal hysteresis. *Nat. Commun.* **7**, 13831 (2016).
19. Harvey, S. P. et al. Mitigating measurement artifacts in TOF-SIMS analysis of perovskite solar cells. *ACS Appl. Mater. Interfaces* **11**, 30911–30918 (2019).
20. Liu, Y., Lorenz, M., Ievlev, A. V. & Ovchinnikova, O. S. Secondary ion mass spectrometry (SIMS) for chemical characterization of metal halide perovskites. *Adv. Funct. Mater.* **30**, 2002201 (2020).
21. Harvey, S. P., Messinger, J., Zhu, K., Luther, J. M. & Berry, J. J. Investigating the effects of chemical gradients on performance and reliability within perovskite solar cells with ToF-SIMS. *Adv. Energy Mater.* **10**, 1903674 (2020).
22. Philippe, B. et al. Chemical distribution of multiple cation (Rb⁺, Cs⁺, MA⁺, and FA⁺) perovskite materials by photoelectron spectroscopy. *Chem. Mater.* **29**, 3589–3596 (2017).
23. Ke, J. et al. In situ investigation of degradation at organometal halide perovskite surfaces by X-ray photoelectron spectroscopy at realistic water vapour pressure. *Chem. Commun.* **53**, 5231–5234 (2017).
24. Sutanto, A. A. et al. 2D/3D perovskite engineering eliminates interfacial recombination losses in hybrid perovskite solar cells. *Chem* **7**, 1903–1916 (2021).
25. Futscher, M. H., Gangishetty, M. K., Congreve, D. N. & Ehrler, B. Quantifying mobile ions and electronic defects in perovskite-based devices with temperature-dependent capacitance measurements: Frequency vs time domain. *J. Chem. Phys.* **152**, 044202 (2020).
26. Du, Y. et al. Electric-field-induced ion migration behavior in methylammonium lead iodide perovskite. *J. Phys. Chem. Lett.* **12**, 7106–7112 (2021).
27. Wu, Y. et al. Formation of MoO₃/organic interfaces. *Adv. Mater. Interfaces* **9**, 2101423 (2022).
28. Jacobsson, T. J. et al. Unreacted PbI₂ as a double-edged sword for enhancing the performance of perovskite solar cells. *J. Am. Chem. Soc.* **138**, 10331–10343 (2016).
29. Shi, L. et al. Gas chromatography-mass spectrometry analyses of encapsulated stable perovskite solar cells. *Science* **368**, eaba2412 (2020).
30. Deepa, M. et al. Cesium power: low Cs⁺ levels impart stability to perovskite solar cells. *Phys. Chem. Chem. Phys.* **19**, 4069–4077 (2017).
31. Kerner, R. A., Xu, Z., Larson, B. W. & Rand, B. P. The role of halide oxidation in perovskite halide phase separation. *Joule* **5**, 2273–2295 (2021).
32. Chen, N., Wang, D., Hu, J., Guan, L. & Lu, Z.-H. Measuring energy gaps of organic semiconductors by electron energy loss spectroscopies. *Phys. Status Solidi (b)* **259**, 2100459 (2022).
33. Wu, S. et al. A chemically inert bismuth interlayer enhances long-term stability of inverted perovskite solar cells. *Nat. Commun.* **10**, 1161 (2019).
34. Khenkin, M. V. et al. Consensus statement for stability assessment and reporting for perovskite photovoltaics based on ISOS procedures. *Nat. Energy* **5**, 35–49 (2020).

35. Domanski, K., Alharbi, E. A., Hagfeldt, A., Grätzel, M. & Tress, W. Systematic investigation of the impact of operation conditions on the degradation behaviour of perovskite solar cells. *Nat. Energy* **3**, 61–67 (2018).

36. Li, J., Dong, Q., Li, N. & Wang, L. Direct evidence of ion diffusion for the silver-electrode-induced thermal degradation of inverted perovskite solar cells. *Adv. Energy Mater.* **7**, 1602922 (2017).

37. Jeangros, Q. et al. In situ TEM analysis of organic-inorganic metal-halide perovskite solar cells under electrical bias. *Nano Lett.* **16**, 7013–7018 (2016).

38. Zhou, Y., Sternlicht, H. & Padture, N. P. Transmission electron microscopy of halide perovskite materials and devices. *Joule* **3**, 641–661 (2019).

39. Chen, Q. et al. Controllable self-induced passivation of hybrid lead iodide perovskites toward high performance solar cells. *Nano Lett.* **14**, 4158–4163 (2014).

40. Yang, X. et al. Buried interfaces in halide perovskite photovoltaics. *Adv. Mater.* **33**, 2006435 (2021).

41. Ni, Z. et al. Evolution of defects during the degradation of metal halide perovskite solar cells under reverse bias and illumination. *Nat. Energy* **7**, 65–73 (2022).

42. Jiang, Q. et al. Planar-structure perovskite solar cells with efficiency beyond 21%. *Adv. Mater.* **29**, 21703852 (2017).

43. Frohna, K. et al. Nanoscale chemical heterogeneity dominates the optoelectronic response of alloyed perovskite solar cells. *Nat. Nanotechnol.* **17**, 190–196 (2022).

44. Futscher, M. et al. Quantification of ion migration in CH$_3$NH$_3$PbI$_3$ perovskite solar cells by transient capacitance measurements. *Mater. Horiz.* **6**, 1497–1503 (2019).

45. Li, B. et al. Understanding the influence of cation and anion migration on mixed-composition perovskite solar cells via transient ion drift. *Phys. Status Solidi RRL* **15**, 2100225 (2021).

46. Vashishtha, P. & Halpert, J. Field-driven ion migration and color instability in red-emitting mixed halide perovskite nanocrystal light-emitting diodes. *Chem. Mater.* **29**, 5965–5973 (2017).

47. Pavlovetc, I. et al. Suppressing cation migration in triple-cation lead halide perovskites. *ACS Energy Lett.* **5**, 2802–2810 (2020).

48. Yamilova, O. et al. Reduction of methylammonium cations as a major electrochemical degradation pathway in MAPbI$_3$ perovskite solar cells. *J. Phys. Chem. Lett.* **11**, 221–228 (2020).

49. Zhang, T. et al. Profiling the organic cation-dependent degradation of organolead halide perovskite solar cells. *J. Mater. Chem. A* **5**, 1103–1111 (2017).

50. Zhang, T., Hu, C. & Yang, S. Ion migration: a "double-edged sword" for halide-perovskite-based electronic devices. *Small Methods* **4**, 1900552 (2020).

51. Lee, J. W. et al. Verification and mitigation of ion migration in perovskite solar cells. *APL Mater.* **7**, 041111 (2019).

52. Heller-Krippendorf, D. *Multivariate Data Analysis for Root Cause Analyses and Time-of-Flight Secondary Ion Mass Spectrometry* (Springer Spektrum Press, Wiesbaden, 2019).

53. Houssiau, L. & Bertrand, P. ToF-SIMS study of organosilane self-assembly on aluminum surfaces. *Appl. Surf. Sci.* **175**, 351–356 (2001).

54. Hu, J. et al. Damage-free depth profiling of electronic structures in multilayered organic semiconductors by photoelectron spectroscopy and cluster ion beam. *Phys. Status Solidi (b)* **258**, 2100130 (2021).

55. Greiner, M. T., Chai, L., Helander, M. G., Tang, W.-M. & Lu, Z.-H. Metal/metal-oxide interfaces: how metal contacts affect the work function and band structure of MoO$_3$. *Adv. Funct. Mater.* **23**, 215–226 (2013).

56. Li, X. et al. Chemical anti-corrosion strategy for stable inverted perovskite solar cells. *Sci. Adv.* **6**, eabd1580 (2020).

Acknowledgements

Author contributions

D.L., R.Z., and Z-H.L. designed the experiments. J.H., D.L., D.W. and N.C. contributed to XPS, UPS and REELS results. J.H., S.Y. and Z.F. conducted the SEM and XRD measurements. P.C. prepared all the samples for film characterizations. P.C., M.Y., L.L. fabricated the PSCs. P.C. characterized photovoltaic performances. D.L., R.Z., and Z.-H.L. directed and supervised the project, J.H. and P.C. wrote the first draft of the paper. D.L. and Z.-H.L. revised paper. All authors analyzed their data, reviewed and commented the paper.

Competing interests

The authors declare no competing interests.

Additional information

Supplementary information The online version contains supplementary material available at https://doi.org/10.1038/s43246-022-00262-2.

Correspondence and requests for materials should be addressed to Deying Luo, Rui Zhu or Zheng-Hong Lu.

Peer review information *Communications Materials* thanks the anonymous reviewers for their contribution to the peer review of this work. Primary Handling Editor: John Plummer.

Reprints and permission information is available at http://www.nature.com/reprints

Publisher's note Springer Nature remains neutral with regard to jurisdictional claims in published maps and institutional affiliations.